Journal of the Australian Ceramic Society
https://doi.org/10.1007/s41779-023-00889-5

RESEARCH

Physico-chemical characterization and in vitro biological study of manganese doped β-tricalcium phosphate-based ceramics for bone regeneration applications

Mehmet Can Arpak[1] · **Sibel Daglilar**[1] · **Cevriye Kalkandelen**[2,3] · **Liliana-Marinela Balescu**[4] · **Hilal Turkoglu Sasmazel**[5] · **Iuliana Pasuk**[4] · **George E. Stan**[4] · **Kagan Durukan**[5] · **Oguzhan Gunduz**[2,6]

Received: 15 November 2022 / Revised: 6 April 2023 / Accepted: 23 April 2023

Abstract

This work evaluates the effects of manganese (Mn) doping on the morpho-structural features, mechanical performance, and in vitro biological response of beta-tricalcium phosphate (β-TCP) derived bioceramics for bone tissue engineering applications. Five different Mn doping levels (i.e., 0.01%, 0.05%, 0.1%, 0.5%, and 1 wt.%) were investigated, with the β-TCP-based bioceramics being sintered at four temperatures (i.e., 1000, 1100, 1200, and 1300 °C). A densification improvement was induced when using Mn in excess of 0.05 wt.%; the densification remained stationary in the sintering temperature range of 1200 – 1300 °C. The structural analyses evidenced that all samples sintered at 1000 and 1100 °C were composed of β-TCP as major phase and hydroxyapatite (HA) as a minor constituent (~ 4–6 wt.%). At the higher temperatures (1200 and 1300 °C), the formation of α-TCP was signalled at the expense of both β-TCP and HA. The Mn doping was evidenced by lattice parameters changes. The evolution of the phase weights is linked to a complex inter-play between the capacity of the compounds to incorporate Mn and the thermal decomposition kinetics. The Mn doping induced a reduction in the mechanical performance (in terms of compressive strength, Vickers hardness and elastic modulus) of the β-TCP-based ceramics. The metabolic activity and viability of osteoblastic cells (MC3T3-E1) for the ceramics were studied in both powder and compacted pellet form. Ceramics with Mn doping levels lower than 0.1 wt.% yielded a more favorable microenvironment for the osteoblast cells with respect to the undoped β-TCP. No cytotoxic effects were recorded up to 21 days. The Mn-doped β-TCPs showed a significant increase ($p < 0.01$) in alkaline phosphatase activity with respect to pure β-TCP.

Keywords Manganese doping · β-tricalcium phosphate · Physical–chemical properties · Rietveld XRD analysis · Cytocompatibility

Introduction

Currently, the frequency of bone tissue disorders, determined by both the increase of life expectancy and by the adoption of a more active lifestyle, has increased considerably [1–4]. Consequently, the demand for osteogenic synthetic materials is on the rise [5–8].

Hydroxyapatite [HA, $Ca_{10}(PO_4)_6(OH)_2$] and β-tricalcium phosphate [β-TCP, $Ca_3(PO_4)_2$] are the most used synthetic materials in bone tissue engineering due to their chemical similarity with the bone mineral component and their excellent biocompatibility [9–11]. β-TCP is known to dissolve faster than HA, which allows for an accelerated growth and healing of the bone [12–14]. This feature made β-TCP attractive for both single use or in combination with HA (i.e., BCPs, biphasic calcium phosphates) in various bone treatment applications [14–16].

Generally, β-TCP can be prepared by thermal conversion (of amorphous calcium phosphates and HA), solid-state reaction, or co-precipitation methods, at temperatures higher than 650–750 °C [17]. β-TCP, once formed, is stable at room-temperature (RT), and transforms into α-TCP phase at temperatures in excess of 1115–1150 °C [17–19]. The areas of application of these two calcium phosphate (CaP) compounds—α- and β-TCP—differ. α-TCP, owned to its ability to hydrate and to set in physiologic conditions [17, 20], became an important component of various bone

---

✉ Oguzhan Gunduz
ucemogu@ucl.ac.uk

Extended author information available on the last page of the article cements, and more rarely used in bi-phasic bioceramics and composites. Instead, β-TCP is considered an invaluable constituent of (ceramic and composite) osteogenic materials [14–16, 21], being both osteoconductive and osteoinductive. Furthermore, the β-TCP addition to bone cements was shown to provide shorter setting times and to increase their mechanical strength [22–24].

Manganese (Mn) is an essential element for bone regeneration [25–33]. Mn positively influences the bone metabolism, augmenting the ligand-ability of integrins (which are mediating the cells interaction with the extra-cellular matrix), promoting the gene levels of alkaline phosphatase, collagen type I, osteocalcin and runt-related transcription factor 2, and supporting cell adhesion, spreading, and proliferation [26, 31, 32, 34–36]. Mn is an essential cofactor for the Glycosyltransferases enzyme [25, 37, 38], and it is important for the extracellular matrix remodelling. Important to note, recently, the Mn-doped β-TCP bioceramics were shown (*i*) to inhibit osteoclastogenesis and to lead to an accelerated bone defect regeneration [26, 29, 39] and (*ii*) to increase of bone mineral density, following in vivo testing (in rat model) [30–32]. Mn is also involved in the metabolism of amino acids, cholesterol, and carbohydrates, helping to maintain the health of the reproductive, nervous and immune systems, and playing a role in blood sugar regulation, blood clotting, and the formation of cartilage and lubricating fluid in the joints [40–42]. Mn sustains the antioxidant defence mechanisms, being efficient in cancer nanomedicine for both diagnosis and treatment [43–46]. Last, but not least, Rau et al. [27, 47] demonstrated that the Mn substitution in β-TCP induces an antibacterial effect, more intense against the Gram-positive strains.

Although the effects of Mn on the environment and the human body have been investigated, its long-term effects are still unknown [48, 49]. Cautionary measures are needed, since Mn can elicit toxicity when used in high doses. It can induce neurodegenerative disorders similar to Parkinson’s disease [25, 50]. While our nervous system can be adversely affected by high manganese intake, various diseases such as skeletal defects, infertility, heart ailments, hypertension, and impaired lipid and carbohydrate metabolism may occur due to its deficiency [40, 42]. Several research reports indicated that the lack of Mn can cause muscle distortion [30]; additionally, skeletal deformities and testicular dysfunction may also occur [28, 42, 50, 51].

In this study, the effects of Mn doping (at low dosages within the range of 0.01–1 wt.%) and sintering temperature (varied in the range of 1000–1300 °C) on the morphological, structural, and in vitro biological properties was explored. Furthermore, for the first time, a special focus was put on the evaluation of mechanical properties (i.e., Vickers hardness, compressive strength, and modulus of elasticity) of these bioceramics. The most promising Mn-doped β-TCP ceramics were delineated by the cross-evaluation of their functional mechanical and in vitro cytocompatibility responses.

Materials and methods

Preparation of simple β-TCP and Mn-doped β-TCP samples

The β-TCP (median particle size: 4 µm) and Mn powders (median particle size: 44 µm) were purchased from Merck and Nanokar Nanotechnology, respectively. Six type of samples were prepared, constituted of pure β-TCP and five different Mn + β-TCP mixtures with 0.01, 0.05, 0.1, 0.5, and 1 wt.% Mn (as shown in Table 1). The accurate weighing of the powders was ensured by using a Radwag AS 60/220.R2 micro-balance with a readability of 0.01 mg, while preparing large size batches (i.e., 50 g, to further minimize the weighting errors). The mixtures were first homogenized by ball milling in ethanol using a RETSCH-S100 equipment, for 240 min at 180 rot/min, then dried in an oven for 2 h at 150 °C. Cylindrical pellets were fabricated by pressing the simple (β-TCP) and ad-mixed (Mn + β-TCP) powders at 350 MPa in stainless steel moulds. Pellets with a diameter/height ratio of 11 mm/11 mm and 11 mm/2 mm were prepared for the mechanical tests and in vitro assays, respectively. Finally, the pellets (from each sample group) were sintered at four different temperatures of 1000, 1100, 1200, and 1300 °C for 4 h, using a Nabertherm LHT 02/17 furnace. Heating and cooling rates of 5 °C/min were used.

Density, morphology, and structure analysis

The bulk density of the sintered ceramic pellets was evaluated by the classical hydrostatic weighting method. The results will be presented as arithmetic means ± standard deviations based on the testing of five individual specimens from each sample group.

The sample morphology was investigated by scanning electron microscopy (SEM) using a Zeiss MA/EVO 10 apparatus operated under the secondary electron mode at

Table 1 Sample codes for powder mixtures

Sample code	β-TCP (wt.%)	Mn (wt.%)
$S_{0.00}$	100	0.00
$S_{0.01}$	99.99	0.01
$S_{0.05}$	99.95	0.05
$S_{0.10}$	99.90	0.10
$S_{0.50}$	99.50	0.50
$S_{1.00}$	99.00	1.00

an acceleration voltage of 10 kV and a working distance of 8–11 mm.

The chemical structure of the ceramics was explored by Fourier Transform Infrared (FTIR) spectroscopy in attenuated total reflectance (ATR) mode, by employing a Perkin Elmer Spectrum BX II spectrometer equipped with a Pike-MIRacle ATR head (Φ1.8 mm) with ZnSe/diamond crystal. The FTIR-ATR spectra were acquired in the range of 2000–500 cm^{-1} at a resolution of 4 cm^{-1}.

The crystalline phase identification was performed by X-ray diffraction in Bragg–Brentano mode, by using a Bruker D8 Advance diffractometer with Cu K_α ($\lambda = 1.5418$ Å) radiation and a LynxEye 1D detector. The patterns were recorded in the 2θ range 15–80°, with a step size of 0.02°. The determination of crystalline phase weights, lattice parameters, and average crystallize sizes was performed by Rietveld refinement [52], by employing the TOPAS v3 software (Bruker AXS), using the fundamental parameter approach. During the whole pattern fitting procedure, the sample displacement parameter was refined and the zero-error of the goniometer was kept constant at zero. The crystallite sizes were refined considering the micro-strain contribution to line broadening.

Mechanical testing

The Vickers micro hardness (HV) tests were carried out at a load of 200 g and a waiting time of 20 s with a Shimadzu HMV-2 system. These analyses were done on triplicate samples, by performing 8 individual measurements on each sample. A Devotrans DVT equipment was employed for the measurement of the compressive strength and the modulus of elasticity. A displacement rate of 2 mm/min was used. These analyses were performed on 5 specimens from each sample group. Subsequently, arithmetic means and standard deviations were calculated.

In vitro biological assays

The cell culture studies were performed on a MC3T3-E1 ATCC CRL-2593 mouse osteoblast cell line, provided by Atılım University (Ankara, Turkey). The cytocompatibility of the β-TCP-based materials sintered at 1000℃ was tested in both powder (using a powder mass/cell culture medium volume of 100 μg/mL) and pelleted form, thus on specimens with dissimilar morphology. Both groups of samples were sterilized under UV for 45 min. The powder specimens were placed into 96-well plates, while the cylindrical pellets were introduced in 24-well plates. The Dulbecco's Modified Eagle Medium/ Nutrient Mixture F-12 (DMEM/F-12) supplemented with 10% v/v foetal bovine serum (FBS), 1% v/v L-glutamine, and 1% v/v penicillin/streptomycin antibiotic solution (all purchased from Amresco, Solon, USA) was used as growth medium. The cell seeding density was of 3×10^3 cells/mL. The samples were incubated under homeostatic conditions (37 °C, 5% CO_2, humidified ambient) up to 21 days. The control of the experiments was constituted by the tissue culture grade polystyrene.

The cell viability/proliferation was tested by 3-(4,5-dimethylthiazol-2-yl)-2,5-diphenyltetrazolium bromide (MTT) assay. Alizarin Red staining was performed to determine calcium deposition, while alkaline phosphates (ALP) activity was inferred to investigate the cell differentiation. The morphology of the cells seeded onto the β-TCP-based pellets was examined by SEM.

Cell viability/proliferation

The MTT assays were performed after 1, 7, 14, and 21 days of cell culturing. After the incubation, the growth medium was removed and the specimens were rinsed three times with phosphate-buffered saline (PBS) solution (Amresco, Solon, USA). After the rinsing process, the specimens in 24-well plates were transferred into a new 96-well plate with 90 μL fresh medium and 10 μL MTT solution (Sigma-Aldrich, USA). For the specimens already in the 96-well plates, the same procedure was applied. After the addition of the MTT solution into the well plates, all samples were incubated for an additional period of 3 h. When the additional incubation time was finalized, the MTT solution was discarded and 200 μL dimethylsulfoxide (DMSO) (Sigma-Aldrich, USA) was added to dissolve the formazan crystals. Again, all samples were incubated for an additional 1 h. Finally, the absorbance values of the solutions were measured with a Dynamica LEDETECT96 microplate reader at 540 nm.

Cell morphology

SEM imaging was performed to inspect the morphology of the cells grown on the β-TCP-based cylindrical pellets. The micrographs were recorded after 7 and 21 days of culturing. To this effect, the specimens were taken from the incubator and the growth medium was discarded. The samples were washed three times with PBS. 10% formalin solution was added to the wells to fixate the cells and then kept in dark, at RT, for 20 min. Thereafter, formalin solution was discarded and cells were washed three times again with PBS. Afterwards the specimens were rinsed with series of ethanol solutions (30–100%) for 2 min each. The specimens were then carefully transferred into a new 24-well plate and treated with 100% hexamethyldisilizane solution for 5 min. Finally, each specimen was fixed onto SEM holders and coated with thin conductive Au-Pt films.

ALP activity

The ALP activity was examined at the 7th, 14th, and 21st day of the cultivation. To form the substrate solution, a nitro blue tetrazolium and 5-bromo-4-chloro-3-indolyl phosphate (NBT/BCIP) tablet (Sigma-Aldrich, USA) was dissolved in 10 mL dH_2O. Thereafter, the prepared solution was kept in dark, at RT, for 2 h. The cultured specimens were removed from the incubator, the growth medium was discarded and the cells were washed three times with PBS. 10% formalin solution was added to the specimens and kept for 1 min to fixate the cells. Afterwards, formalin solution was discarded and cells were washed again three times with PBS. Finally, the substrate solution was added to the wells, incubated at RT for 10 min, and measurements were carried out at 405 nm using the Dynamica LEDETECT96 microplate reader.

Alizarin Red staining

An Alizarin Red staining test (Sigma-Aldrich, USA) was carried out for the characterization of calcium deposition in the cells seeded on the pelleted specimens, after the 7th, 14th, and 21st day of the cultivation. To obtain the staining solution, 2 g of Alizarin Red stain was dissolved in 10 mL of deionized water (dH_2O) and the final pH was set to 4.1–4.3 via HCl. The final solution was stored in dark until use. After incubation (5% CO_2, 37 °C), the culture medium was removed and the specimens were rinsed with PBS solution. The fixation of the cells was done by 10% formalin addition and the specimens were kept in dark for 30 min. Further, the formalin was carefully discarded and the cells were washed with deionized water. Thereafter the stain solution was added onto the specimens which were kept in dark at RT for 30 min. Subsequently, the samples were centrifuged at a speed of 200 rot/min. Finally, the absorbance values of the solutions were measured at 405 nm via Dynamica LEDETECT96 microplate reader to characterize the level of calcium deposition/mineralization.

Results and discussion

Density, morphological, and structural characterization

Figure 1 shows the evolution of the density of the bioceramics with the sintering temperature. A low compactization of all ceramics was noticed for the 1000 °C sintering regime, yielding density values in the range of ~ 2.2–2.3 g/cm^3, irrespective of Mn content. An important increase of density was noticed for all ceramics after the 1100 °C sintering, with emphasis on the β-TCP-based ceramics containing Mn in excess of 0.01 wt.%. The density of the ceramics was further increased at 1200 °C, and experienced only marginal modifications at 1300 °C, regardless of the Mn concentration. Still, it can be noted that the highest density value of ~ 2.77 g/cm^3 was reached in the case of the 0.05 wt.% Mn-doped ceramics, sintered at 1300 °C. The relative density of β-TCP is being frequently reported to be close to 3.07 g/cm^3 [17]. The results are similar with those reported by Ryu et al. and Turan et al. [53, 54].

The morphological analysis was carried out only for the β-TCP-based ceramics sintered at 1000 and 1300 °C (Fig. 2). All the 1000 °C sintered ceramics presented intergranular pores, with seemingly lower numbers in the case of the 0.05 and 0.1 wt.% Mn-doped β-TCP-based ceramics. As expected, higher densifications (with no or sporadic pores only) and larger grain sizes are induced by a higher temperature sintering. After the 1300 °C sintering, larger grains (i.e., ~ 10–25 µm) were obtained for the same 0.05 and 0.1 wt.% Mn-doped samples (with respect to pure β-TCP). Lower grain sizes (i.e., ~ 2.5–8 µm) were observed

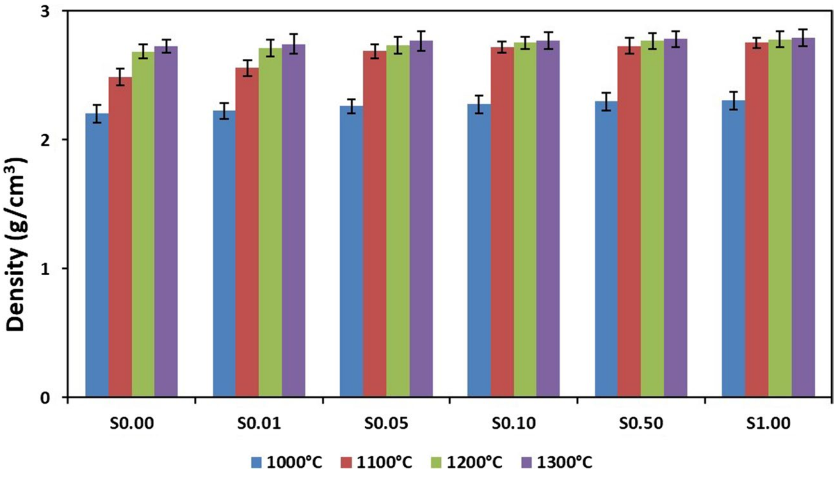

Fig. 1 Density values of the simple and Mn-doped β-TCP-based ceramic pellets sintered at temperatures of 1000, 1100, 1200, and 1300 °C

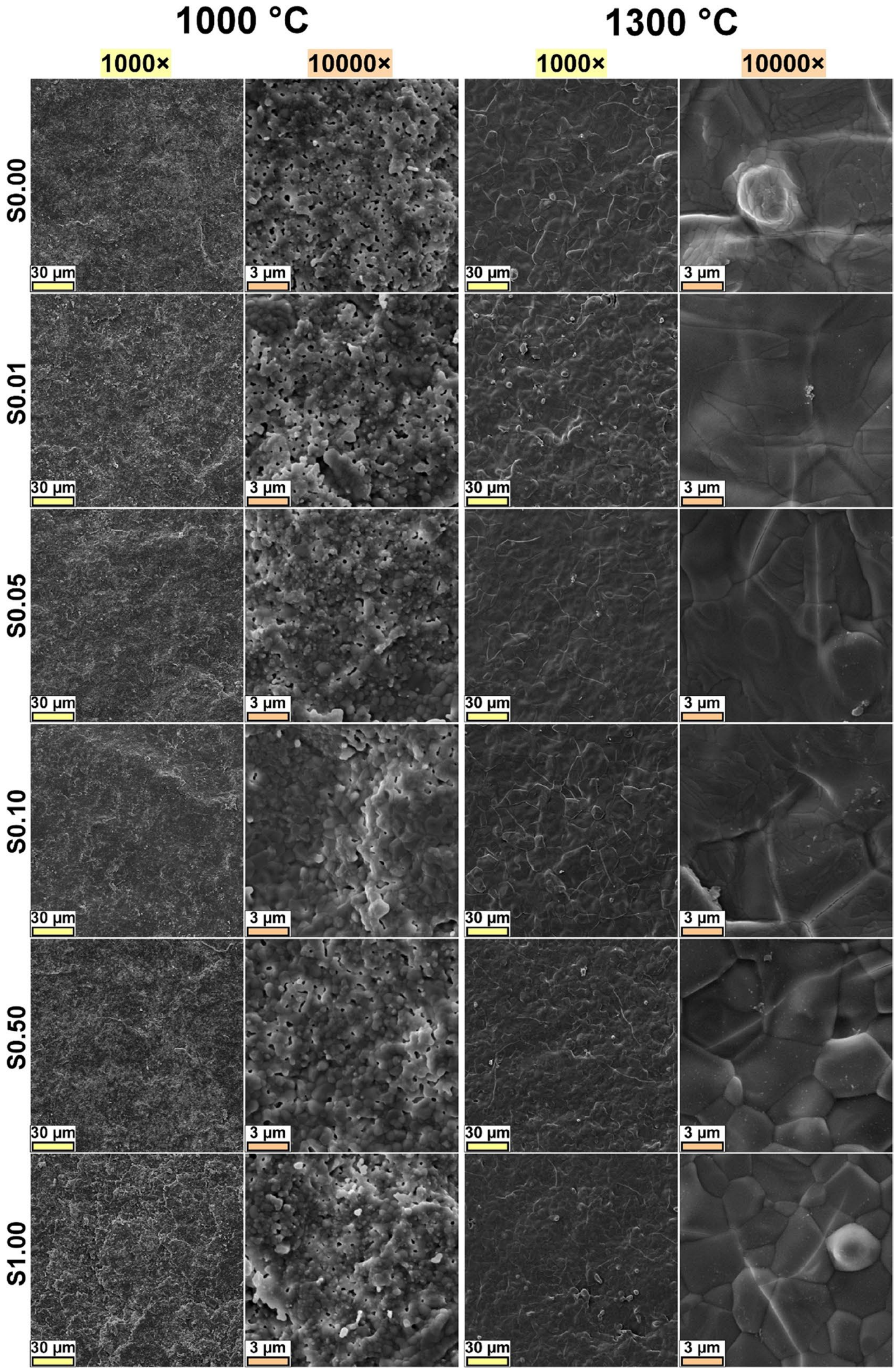

Fig. 2 SEM images of the β-TCP-based samples sintered at 1000 °C and 1300 °C

for the samples doped with 0.5 and 1 wt.% of Mn (Fig. 2 – 1000 × micrographs).

Figure 3 presents the FTIR-ATR spectra of the β-TCP-based ceramics in comparison to the IR spectrum of the commercially pure β-TCP reference material (Sigma-Aldrich, CAS no. 7758–87-4). The Mn doped β-TCP samples featured spectral envelopes analogous to β-TCP control material, suggesting that β-TCP is the prominent constituent of all specimens, regardless of their doping level or sintering temperature. The presence of all IR bands characteristic to a β-TCP compound were evidenced: i.e., ν_4 triply degenerated asymmetric bending (at ~ 540 and 600 cm^{-1}), factor group splitting of ν_1 symmetric stretching (at ~ 943 and 968 cm^{-1}), and the ν_3 triply degenerated asymmetric stretching (at ~ 1015, 1036, 1081, and 1116 cm^{-1}) vibration modes [55, 56].

The XRD patterns of the β-TCP-based ceramics are comparatively presented in Fig. 4. Although the patterns were recorded in the 2θ range of 15–80°, for the graphical presentation, a more confined 2θ range was preferred (i.e., 15–45°) such as to enable the better visualization of the peaks and their assignment. The phase composition

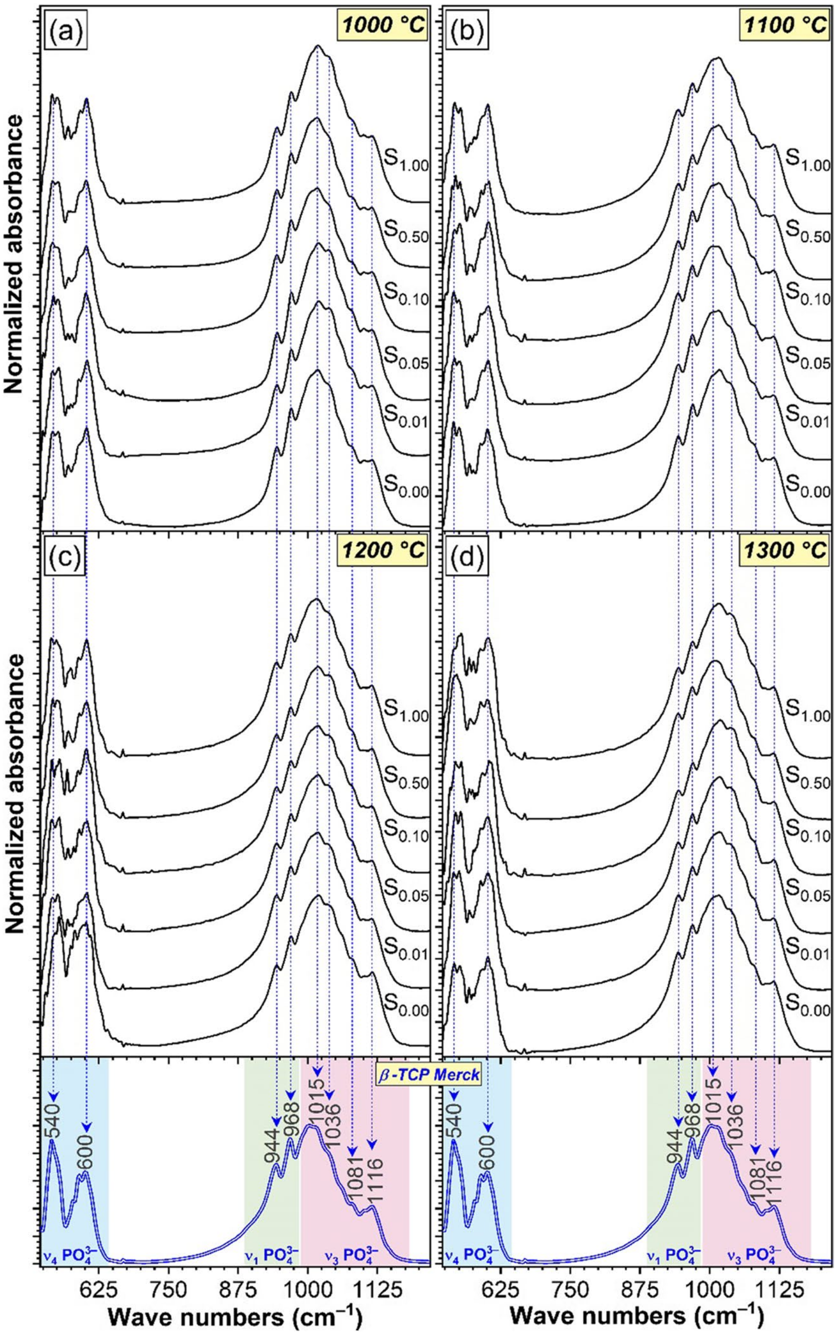

Fig. 3 The FTIR-ATR spectra of the simple and Mn-doped β-TCP-based ceramics sintered at (**a**) 1000 °C, (**b**) 1100 °C, (**c**) 1200 °C, and (**d**) 1300 °C. The spectrum of the pure commercial β-TCP powder (Sigma-Aldrich, CAS no. 7758–87-4, purity ≥ 98%) is presented (with blue line) for comparison at the bottom of the graphs

Fig. 4 The XRD patterns of the simple and Mn-doped β-TCP-based ceramics sintered at (**a**) 1000 °C, (**b**) 1100 °C, (**c**) 1200 °C, and (**d**) 1300 °C. The ICDD reference files of the hexagonal HA (in red), rhombohedral β-TCP (in blue), and monoclinic α-TCP (in green) phases are represented for comparison as sticks at the bottom of the graphs

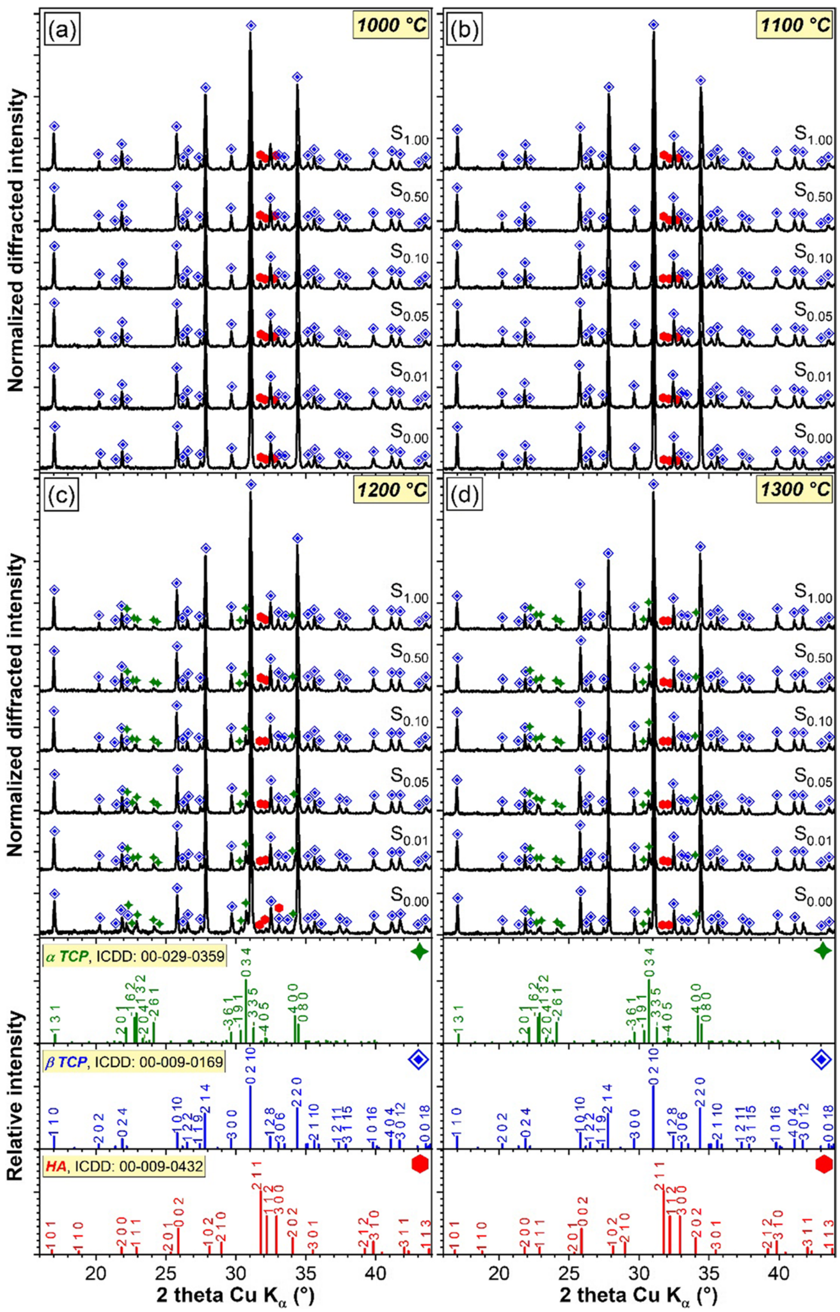

of each specimen, as determined by Rietveld whole pattern fitting, is given in Fig. 5 (the starting structures for the Rietveld refinements were as follows: β-TCP – ICSD no. 97500; HA – ICSD no. 87670; and α-TCP – ICSD no. 923). The samples heat-treated at 1000 °C and 1100 °C were composed of β-TCP (as major phase, with a share of ~ 94–96 wt.%) and HA (as minor phase, with a share of ~ 4–6 wt.%). No noteworthy phase composition changes were recorded in this temperature range with the Mn doping. In good agreement with the thermal decomposition kinetics of β-TCP, at temperatures higher than ~ 1125 °C [9, 17, 18] (i.e., samples heat-treated at 1200 °C and 1300 °C), the presence of α-TCP (~ 8–17 wt.%) was observed. The emergence of α-TCP is accompanied by the decrease of both β-TCP and HA phases (following the HA → β-TCP → α-TCP thermal decomposition chain) [9, 17, 18]. The Mn doping appears to mitigate the decomposition of β-TCP at 1200 °C (Fig. 5a). The stabilizer role of Mn on the β-TCP lattice was seemingly overpowered at the sintering temperature of 1300 °C by the thermal β-TCP → α-TCP decomposition kinetics. At this temperature, the β-TCP concentration showed a continuous decrease with Mn content, while the α-TCP experienced an equivalent weight increase.

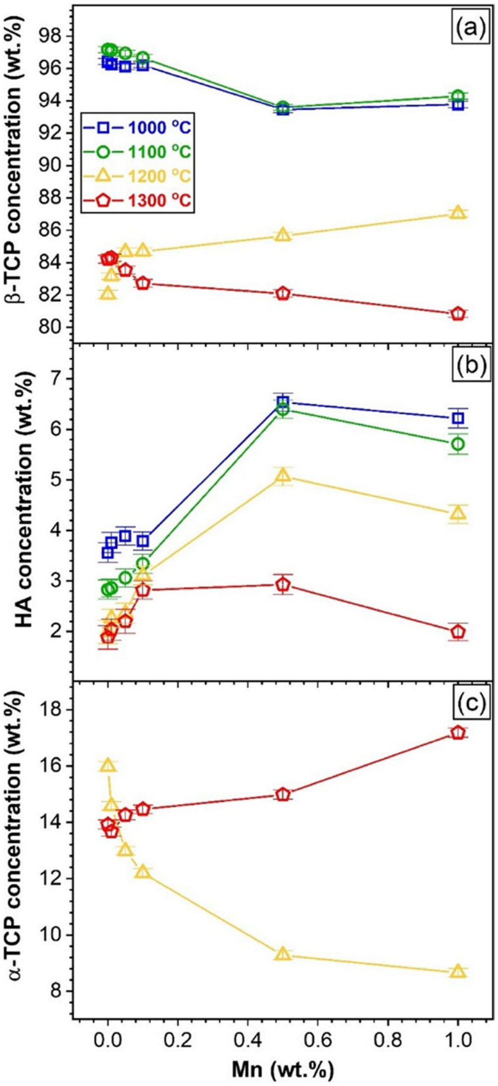

Fig. 5 Evolution of phase composition of (**a**) β-TCP; (**b**) HA; and (**c**) α-TCP as a function of Mn concentration for the samples sintered at 1000, 1100, 1200, and 1300 °C, as determined by Rietveld whole pattern fitting

A decrease in α-TCP concentration (with the increase of the sintering temperature from 1200 to 1300 °C) was recorded only in the case of the non-doped and lower Mn-doped β-TCP samples (i.e., S0.01). It is to note that typically the α-TCP phase is metastable at RT, and its conversion to β-TCP has been reported [57–59]. One hindering approach is to (*i*) rapidly quench the samples during synthesis to room-temperature or (*ii*) to use of various dopants to stabilize its crystalline phase [57–59]. Taken together all this information seem to suggest that in the absence or at low concentration of Mn (i.e., 0.01 wt.%), the α-TCP phase remains metastable, leading to its conversion to β-TCP upon cooling after the higher temperature sintering (Fig. 5 a,c). Seemingly, the further increase of Mn consequents in a gradual stabilization of the α-TCP phase, manifested by its progressive concentration increase (Fig. 5c).

Matsunaga et al. [60] showed by first-principles density functional theory calculations, at RT, that divalent ions (Mn not included) are more stable in the β-TCP lattice than in the α-TCP one, with possible consequences on the solubility behaviour in physiological fluids. However, our experimental data highlighted rather different trends, probably owned to the supplemental contribution of the high sintering temperature to the decomposition kinetics of β-TCP. In fact, as it will be detailed further, Mn seems to be progressively incorporated into α-TCP, stabilizing it against β-TCP. The phase evolution in our Mn-doped ceramics could be ascribed to an inter-play between the capacity of the three constituting CaP phases to incorporate Mn and the effect of their doping on the thermal decomposition kinetics.

Given that there is a quite large difference between the ionic radii of Mn^{2+} and Ca^{2+} (Mn^{2+} ranges from 80 to 97 pm, depending on coordination, while Ca^{2+} ranges between 114 and 126 pm, according to https://www.webelements.com/), the Mn substitution for Ca in any of the crystalline CaPs identified in these samples (i.e., HA, β-TCP, or α-TCP) would cause the decrease of the unit cell. The evolution of the lattice parameters of these phases, as a function of Mn content, for samples obtained at different sintering temperatures are represented in Fig. 6.

The sintering regime had a more pronounced effect on the lattice parameters with respect to the Mn doping. For β-TCP, the *a*-constant increased and the *c*-constant decreased with the temperature, while for HA, the reverse was noticed, with the *a*- and *c*-constants decreasing and increasing, respectively. Another inversion was observed for the β-TCP phase when increasing the sintering temperature from 1000 to 1100 °C. A similar lattice parameters behaviour with temperature was reported by Gibson et al. [61], being ascribed by changes/distortions in orthophosphate tetrahedra. Concerning the dependence on the Mn amount, one can observe an almost general behaviour: at very low Mn concentrations, both the *a*- and *c*-lattice constants decreased at each sintering temperature. At higher concentrations, the variation with Mn is faint, and the trend differs for each sintering temperature. For the major β-TCP phase, at the 1000 and 1100 °C, the *a*-constant decreased monotonously as the Mn concentration increased from 0.1 to 1 wt.%. At the same temperature, the *c*-constant varied in a less consistent manner with Mn, but also suggested, on the average, a similar decreasing trend. At the same time, the *a*-constant of the coexistent HA phase markedly decreased as the Mn increased, especially at 1000 °C. This indicates that Mn was incorporated in both β-TCP and HA lattices, at these low sintering temperatures (i.e., 1000 and 1100 °C). Interestingly, the quantitative phase composition estimations (Fig. 5) showed that the presence of Mn has not boosted the HA decomposition into β-TCP, as

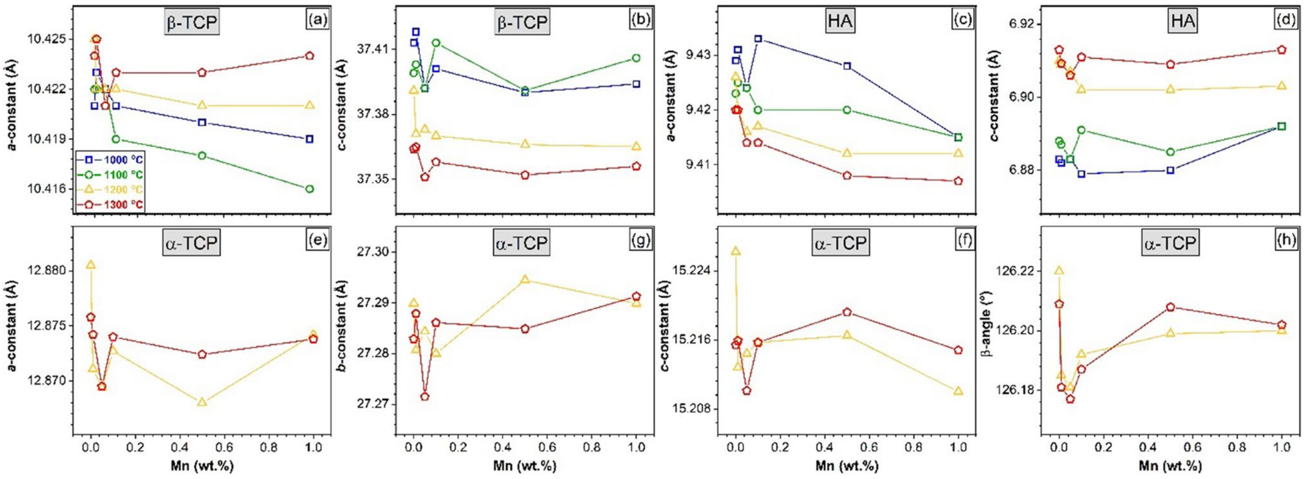

Fig. 6 Evolution of lattice parameters of the (**a, b**) β-TCP; (**c, d**) HA; and (**e–h**) α-TCP constituting phases as a function of Mn concentration for the samples sintered at 1000, 1100, 1200, and 1300 °C, as determined by Rietveld whole pattern fitting

other authors have suggested [27, 62]. At 1200 and 1300 °C, the HA lattice seemed to remain sensible to the Mn amount in the samples, indicating that at these temperatures the Mn incorporation in HA is still consistent. With the emergence of α-TCP at higher temperatures, Mn founds a third host, and thus, the structural scenario gets more complicated. The intake of Mn in α-TCP was evidenced by the decrease of its lattice parameters with the amount of dopant. Once Mn is shared also with the abundant α-TCP phase, it becomes less available for β-TCP. Consequently, at 1200 °C (where α-TCP emerged), the lattice parameters of β-TCP no longer vary with the Mn concentration. At 1300 °C, where the samples showed a considerable enrichment in α-TCP phase, markedly for Mn contents higher than 0.5 wt.%, the lattice parameters of β-TCP experienced a slight increase (towards the values corresponding to the undoped sample). This could supposedly be linked to the β-TCP depletion in Mn, in favor of α-TCP. This apparently contrasts to what is generally reported in literature. However, no studies on the evolution of Mn-doped CaP-based materials at temperatures higher than 1100 °C were yet reported to the best of our knowledge. Indeed, at intermediate sintering temperatures (650 – 850 °C) [63] and high Mn concentrations (e.g., 5 at.%) [62], the β-TCP can be stabilized.

The evolution of the crystallite sizes of the major β-TCP phase with the Mn content, at different sintering temperatures, is represented in Fig. 7. The dependence of the β-TCP crystallite size on the Mn amount was found rather weak and inconsistent. An increase of the average crystallite size with temperature was observed, in good agreement with the grain growth revealed by SEM (Fig. 2). The mean crystallite size of α-TCP has grown from ~ 80–99 to ~ 86–129 nm with the increase of sintering temperature from 1200 to 1300 °C. In the case of HA, the crystallite sizes remained rather insensible to both Mn doping and sintering temperature, with values situated in the range of ~ 70–100 nm.

Mechanical performance

The evolution of the microhardness, compressive strength, and elastic modulus of the β-TCP-based ceramics, sintered at different temperatures, is shown in Fig. 6. The higher compressive strength results (77–143 MPa) were obtained for the samples sintered at 1000℃ and 1100℃. These values are similar to those reported by Tian et al. [64]. The increase of the sintering temperature to 1200℃ and 1300℃ resulted into a decrease of the compressive strength values of the samples with Mn doping levels higher than 0.05 wt.% to ~ 70 and ~ 60 Mpa, respectively. The hardness values of the ceramics were higher for the 1000℃ treated samples (with the exception of the pure β-TCP, which presented a maximum of ~ 745 HV

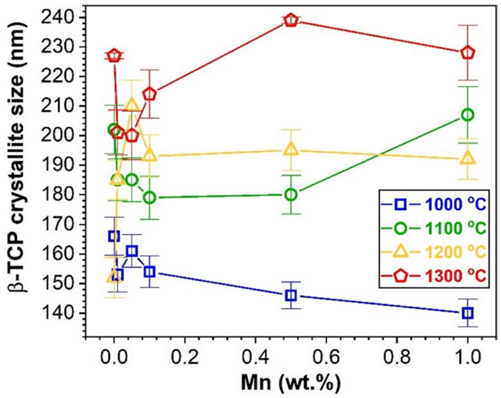

Fig. 7 Evolution of crystallite size of the β-TCP as a function of Mn concentration at different sintering temperatures (1000, 1100, 1200, and 1300 °C), as determined from XRD

after the 1000 °C sintering). A decrease of microhardness with the increase of Mn content and sintering temperature was noticed. Similarly, to the hardness trends, higher elastic modulus values were generally yielded by the samples sintered at 1000 and 1100 °C. Generally, Mn addition reduced the elastic modulus of the bio-ceramics. The lowest modulus of elasticity was consistently observed at the highest sintering temperature.

Cell culture studies

Metabolic activity and viability

The metabolic activity and viability of the MC3T3-E1 cells in the presence of pure and Mn-doped β-TCP-based samples (in powdered and pelleted form) were investigated. No cytotoxic effects were recorded for any of the samples up to 21 days. At day-21st, all Mn-doped β-TCP-based pellets showed a higher cell viability compared to both the biological control and the pure β-TCP ($p < 0.01$).

In addition, the highest cell viability was exhibited by the 0.05 wt.% Mn-doped sintered cylindrical β-TCP-based pellets. Thereby, it can be presumed that such a Mn-doped β-TCP-based bio-ceramic constitutes an appropriate surface for the development of osteoblast cells (Fig. 7a).

On the other hand, at day 21st, the 0.01 and 0.1 wt.% Mn-doped β-TCP powdered specimens showed a similar cell viability compared to the tissue culture grade polystyrene control ($p < 0.01$) (Fig. 7b). This provided a supplemental clue that a β-TCP with low Mn doping (in this case, in powdered form) could serve as a favourable microenvironment for the osteoblast cells.

Furthermore, according to the SEM data, all surfaces of the Mn-doped β-TCP-based sintered pellets were covered with osteoblast cells. A higher cell density compared to the other β-TCP-based pellets was observed in the case of the $S_{0.05}$-type samples (Fig. 8), in good agreement with the MTT results (Fig. 7a).

Mn is an important micronutrient which has a critical role for human body, being recognized to influence the adhesion of cells to extracellular matrix proteins [65]. The cytotoxicity and enhancing effects of the Mn are dose dependent. When used in low concentrations, the Mn ions improve cell viability, proliferation, and differentiation [25, 27, 65, 66]. Westhauser et al. [66] prepared a Mn-doped (5 mol%) mesoporous bioactive silica-based glass, performed tests in human marrow-derived mesenchymal stromal cells, and showed this material's capacity to boost the pro-osteogenic features. Torres et al. [25] synthesized compositional series of Mn-substituted β-TCPs, carried out in vitro biological tests in MC3T3-E1 osteoblast cells cultures, and indicated that the biological benefits emerge at a lower concentration (0.76 mol%) of Mn incorporated in β-TCP. Lüthen et al. [65] studied the effect of divalent Mn cations (using as source $MnCl_2$ in a concentration range of 0.01–0.5 mM) on MG-63 osteoblastic cells. They indicated that at concentrations higher than 0.1 mM $MnCl_2$ the expression of both alkaline phosphatase (ALP) and collagen 1 (Col 1) mRNA decreased. Rau et al. [27] tested the biological properties of pure and Mn-doped β-TCP (i.e., $Mn_xCa_{3-x}(PO_4)_2$, with $x = 0.001$, 0.01, and 0.1). They found that the β-TCP with the lowest Mn doping, thus leaching more reduced amounts of Mn^{2+}, was able to induce the most marked differentiation of adipose-derived mesenchymal stem cells towards three different phenotypes: osteogenic, adipogenic, and chondrogenic.

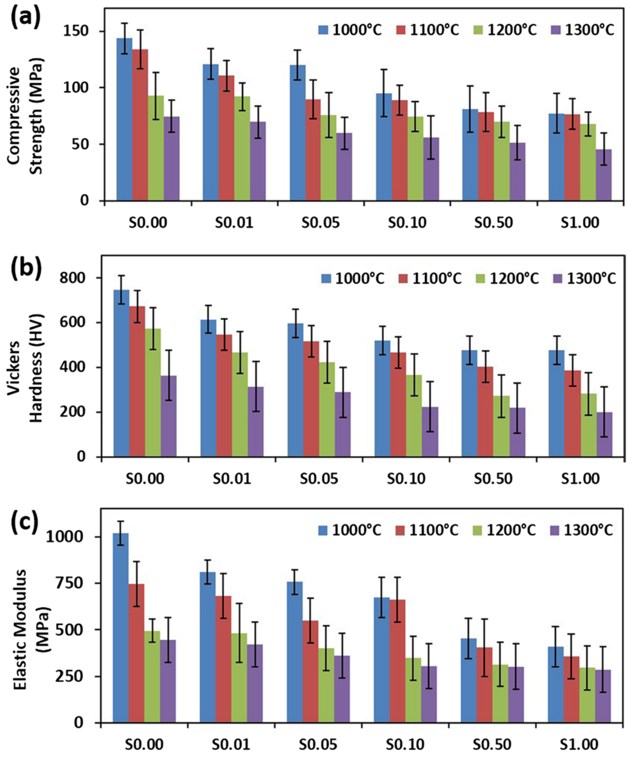

Fig. 8 Mechanical testing results: the (**a**) compressive strength; (**b**) Vickers hardness; and (**c**) elastic modulus of β-TCP-based samples sintered at 1000, 1100, 1200, and 1300 °C

In our study, concentrations of Mn lower than 0.1 wt.% created the most favourable microenvironment for the osteoblast cells. The β-TCP-based materials with Mn concentration higher than 0.1 wt.% were less auspicious and thereby, the cell viability fluctuated at each incubation day.

Osteoblastic and osteogenic differentiation

The pre-osteoblastic differentiation was determined by an ALP activity test, surveying the inorganic phosphate accumulation. The ALP activity results of the pure and Mn-doped β-TCP-based sintered pellets, after 7, 14, and 21 days of culturing, are shown in Fig. 9a. All β-TCP-based materials

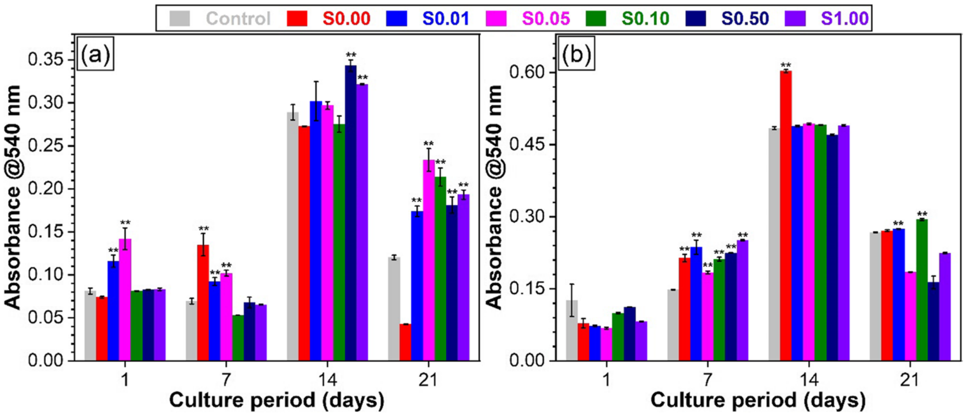

Fig. 9 Viability of MC3T3-E1 cells cultured in the presence of pure and Mn-doped β-TCP-based sintered ceramics in form of (**a**) cylindrical pellets and (**b**) powder specimens. Statistically significant differences are shown by '*', '**', '***', and '****' denoting p-values < 0.05, 0.01, 0.001, and 0.0001, respectively

showed a significant ($p < 0.01$) increase in terms of ALP activity after 14 days with respect to the tissue culture grade polystyrene control. However, after 21 days, the biological control exhibited a higher ALP activity compared to the pure and Mn-doped β-TCP-based pellets. This might be caused by the differentiation normalization of the Mn-doped bioceramics. In addition, the differentiation maximum for the biological control occurred later than for the Mn-containing β-TCP-based materials, which is an indication for the enhancement of the pre-osteoblastic differentiation by Mn doping. Overall, lower concentrations of Mn were found favourable for pre-osteoblastic differentiation, in good agreement with the studies performed by Wu et al. [26] and Li et al. [39].

The mineralization capability of the simple and Mn-substituted β-TCP-based bioceramics was inferred by evaluating calcium deposits via Alizarin Red staining after 7, 14, and 21 days of cell culturing (Fig. 9b). A slight increase in terms of mineralization, with peaks on the 14th day and 21st day, was noticed. On day 21st, all specimens exhibited significantly higher values ($p < 0.01$) in terms of mineralization compared to the tissue culture grade polystyrene control. In addition, the highest mineralization value was induced by pure and the $S_{0.05}$ Mn-doped (0.05 wt.%) sintered β-TCP-based pellets (Figs. 10, 11).

By joint assessment, the mineralization results and the ALP activity indicated that the most sustainable and beneficial microenvironment for osteoblast cells viability, proliferation, differentiation, and mineralization was provided by the $S_{0.05}$-type sample (thus with 0.05 wt.% Mn content). The delineation of an optimum Mn substitutional level in calcium phosphate bioceramics, could prove of great importance, since it could enable the increase of ALP activity and mineralization, and further enhance the bone morphogenetic protein 2 (BMP-2) expression [39, 67]. BMP-2 can induce the differentiation of osteoblasts into an assortment of cell types and it is known to play a role of paramount importance in the formation of bone and cartilage tissues.

Previous studies have shown that manganese (Mn) ions can improve bone regeneration and can be used in the treatment of osteoporosis. However, there are still conflicting evidences with respect to the recommended Mn dosage in CaP ceramics. Consequently, we have adopted a new doping approach, by employing metallic Mn instead of traditionally use metal oxides (furthermore as manganese oxide has numerous polymorphs) as doping agent. This might pave the road towards more predictable fabrication procedures and overall functional responses of such bio-ceramics. In this respect, multi-parametrical physico-chemical and in vitro biological analyses were devoted to delineate suitable Mn-doped CaP-based bio-ceramics.

Conclusions

A series of conclusions can be drawn from this study:

1. The density of the samples increased with the sintering temperature. The density was observed with the addition of Mn up to 0.05 wt.% only in the case of the 1100 °C sintered samples. Since it is thought that it is very close to the saturation point at this point, subsequent increases have remained relatively low.
2. The SEM analyses indicated that the 0.05 and 0.1 wt.% Mn-doped samples had larger grains (i.e., ~ 10–25 µm), while the highly Mn-doped ceramics (i.e., 0.5 and 1 wt.%) presented the lower grain sizes (i.e., ~ 2.5–8 µm).
3. The structural analyses showed that, at low sintering temperatures (1000–1100 °C), all bioceramics were constituted of β-TCP and HA, as major (~ 94–96 wt.%) and minor (~ 4–6 wt.%) highly-crystallized phases, respectively. At the high temperatures sintering (1200 and 1300 °C) the formation of α-TCP (~ 8–17 wt.%) was noticed, at the expense of both β-TCP and HA. At 1300 °C, the stabilizer role of Mn was overcome by the β-TCP → α-TCP thermal decomposition kinetics. The phase evolution could be ascribed to an intricate interplay between the capacity of the three constituting CaP

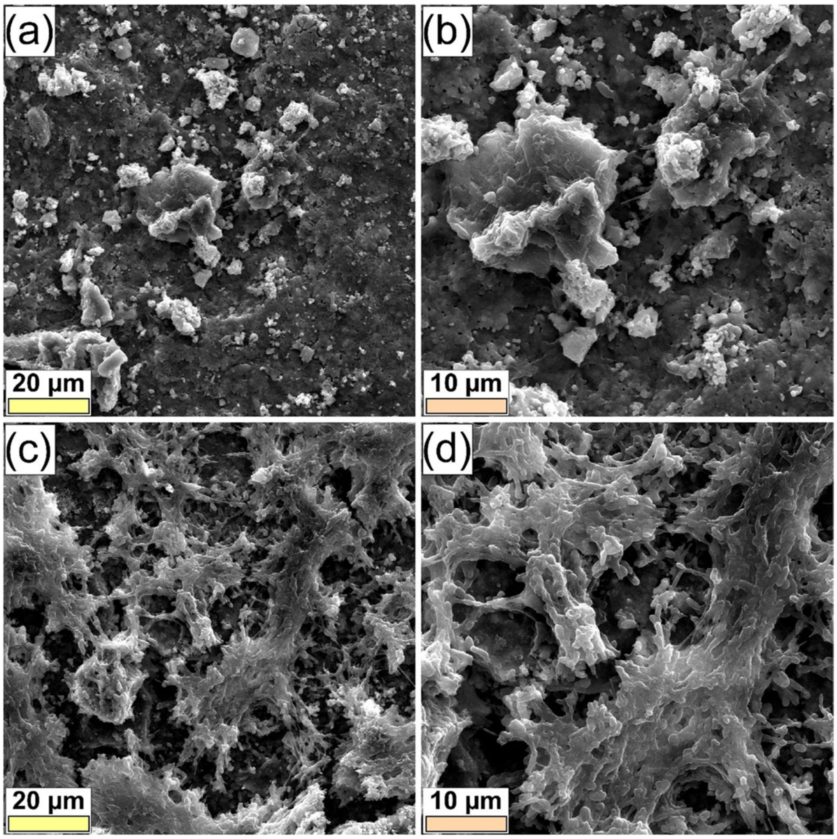

Fig. 10 SEM images collected on the surface of the $S_{0.05}$ Mn-doped β-TCP-based sintered pellets incubated with MC3T3-E1 cells for (**a, b**) 7 and (**c, d**) 21 days. Magnification: (**a, c**) 2500×; (**b, d**) 5000×

phases to incorporate Mn and the effect of their doping on the thermal decomposition kinetics.

4. The mechanical properties (compressive strength, Vickers hardness, and elastic modulus) declined with the increase of Mn content.
5. Mn is a dose dependent micronutrient which influences cell adhesion. Accordingly, 0.05 wt.% Mn-doped sintered β-TCP-based materials exhibited the highest cell viability amongst the Mn-compositional series. No cytotoxic effects towards osteoblasts were recorded up to 21 days, irrespective of Mn content. At day-21^{st}, all Mn-doped β-TCP-based ceramics elicited a higher cell viability with respect to both the control and the pure β-TCP samples.
6. After 14 days, the Mn-doped d β-TCP ceramics induced a more significant osteoblast differentiation compared to the biological control. However, after 21 days of cell culturing the differentiation normalized, leading to values similar to the biological control, which suggested a Mn-induced enhancement of the pre-osteoblastic differentiation. Taken together, the viability/proliferation, differentiation and mineralization assays indicated that the most sustainable and beneficial microenvironment for the osteoblast cells was provided by the $S_{0.05}$-type

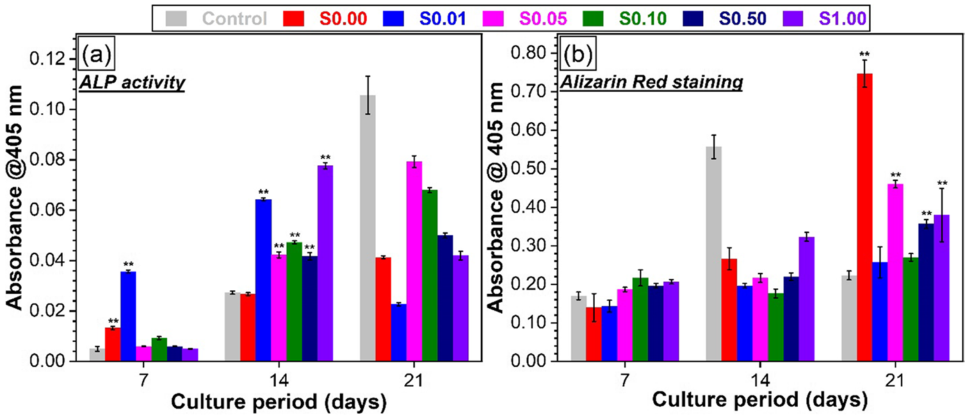

Fig. 11 Osteogenic differentiation and mineralization of MC3T3-E1 cells cultured on the pure and Mn-doped β-TCP-based sintered pellets ceramics: (**a**) ALP activity and (**b**) Alizarin Red staining absorbance values read at 405 nm. Statistically significant differences are shown by '*', '**', '***', and '****' denoting *p*-values < 0.05, 0.01, 0.001, and 0.0001, respectively

sample (thus with a 0.05 wt.% Mn content). It is thus suggested that such Mn-containing bioceramics hold certain promise for promoting bone regeneration in osteoporosis treatment.

Acknowledgements G.E.S. and L.M.B. are thankful for the financial support of the Romanian National Authority for Scientific Research and Innovation, CNCS-UEFISCDI, in the framework of PNIII-P1-1.1-TE-2019-0463 project (within PNCDI III), as well as to Core Program of the National Institute of Materials Physics within the National Research Development and Innovation Plan 2022–2027, carried out with the support of the Romanian Ministry of Research, Innovation and Digitalization under the project PC2-PN23080101.

Declarations

Conflict of interest The authors declare no competing interests.

References

1. Dayer, S.R., Mears, S.C., Pangle, A.K., Mendiratta, P., Wei, J.Y., Azhar, G.: Does superior bone health promote a longer lifespan? Geriatr. Orthop. Surg. Rehabil. **12**, 215145932110362 (2021). https://doi.org/10.1177/21514593211036231
2. Salari, N., Darvishi, N., Bartina, Y., Larti, M., Kiaei, A., Hemmati, M., Shohaimi, S., Mohammadi, M.: Global prevalence of osteoporosis among the world older adults: a comprehensive systematic review and meta-analysis. J. Orthop. Surg. Res. **16**, 669 (2021). https://doi.org/10.1186/s13018-021-02821-8
3. Oden, A., Dawson, A., Dere, W., Johnell, O., Jonsson, B., Kanis, J.A.: Lifetime risk of hip fractures is underestimated. Osteoporos. Int. **8**, 599–603 (1998). https://doi.org/10.1007/s001980050105
4. World Health Organization - Life expencancy and healthy life expectancy, (2022). https://www.who.int/data/gho/data/themes/mortality-and-global-health-estimates/ghe-life-expectancy-and-healthy-life-expectancy (accessed November 28, 2022).
5. Koons, G.L., Diba, M., Mikos, A.G.: Materials design for bone-tissue engineering. Nat. Rev. Mater. **5**, 584–603 (2020). https://doi.org/10.1038/s41578-020-0204-2
6. Qu, H., Fu, H., Han, Z., Sun, Y.: Biomaterials for bone tissue engineering scaffolds: a review. RSC Adv. **9**, 26252–26262 (2019). https://doi.org/10.1039/C9RA05214C
7. Tang, G., Liu, Z., Liu, Y., Yu, J., Wang, X., Tan, Z., Ye, X.: Recent trends in the development of bone regenerative biomaterials. Front. Cell Dev. Biol. **9**, 665813 (2021). https://doi.org/10.3389/fcell.2021.665813
8. Montoya, C., Du, Y., Gianforcaro, A.L., Orrego, S., Yang, M., Lelkes, P.I.: On the road to smart biomaterials for bone research: definitions, concepts, advances, and outlook. Bone Res. **9**, 12 (2021). https://doi.org/10.1038/s41413-020-00131-z
9. Jeong, J., Kim, J.H., Shim, J.H., Hwang, N.S., Heo, C.Y.: Bioactive calcium phosphate materials and applications in bone regeneration. Biomater. Res. **23**, 4 (2019). https://doi.org/10.1186/s40824-018-0149-3
10. Lu, J., Yu, H., Chen, C.: Biological properties of calcium phosphate biomaterials for bone repair: A review. RSC Adv. **8**, 2015–2033 (2018). https://doi.org/10.1039/c7ra11278e
11. Tite, T., Popa, A.C., Balescu, L.M., Bogdan, I.M., Pasuk, I., Ferreira, J.M.F., Stan, G.E.: Cationic substitutions in hydroxyapatite: Current status of the derived biofunctional effects and their in vitro interrogation methods. Materials (Basel). **11**, 2081 (2018). https://doi.org/10.3390/ma11112081
12. Wang, L., Nancollas, G.H.: Calcium orthophosphates: Crystallization and dissolution. Chem. Rev. **108**, 4628–4669 (2008). https://doi.org/10.1021/cr0782574
13. Dorozhkin, S.V.: Calcium orthophosphates: occurrence, properties, biomineralization, pathological calcification and biomimetic applications. Biomatter. **1**, 121–164 (2011). https://doi.org/10.4161/biom.18790
14. Gallinetti, S., Canal, C., Ginebra, M.P.: Development and characterization of biphasic hydroxyapatite/β-TCP cements. J. Am. Ceram. Soc. **97**, 1065–1073 (2014). https://doi.org/10.1111/jace.12861
15. Bouler, J.M., Pilet, P., Gauthier, O., Verron, E.: Biphasic calcium phosphate ceramics for bone reconstruction: A review of biological response. Acta Biomater. **53**, 1–12 (2017). https://doi.org/10.1016/j.actbio.2017.01.076
16. Basu, S., Basu, B.: Unravelling doped biphasic calcium phosphate: Synthesis to application. ACS Appl. Bio Mater. **2**, 5263–5297 (2019). https://doi.org/10.1021/acsabm.9b00488
17. Bohner, M., Santoni, B.L.G., Döbelin, N.: β-tricalcium phosphate for bone substitution: Synthesis and properties. Acta Biomater. **113**, 23–41 (2020). https://doi.org/10.1016/j.actbio.2020.06.022
18. Carrodeguas, R.G., De Aza, S.: α-Tricalcium phosphate: Synthesis, properties and biomedical applications. Acta Biomater. **7**, 3536–3546 (2011). https://doi.org/10.1016/j.actbio.2011.06.019
19. Safronova, T.V., Selezneva, I.I., Tikhonova, S.A., Kiselev, A.S., Davydova, G.A., Shatalova, T.B., Larionov, D.S., Rau, J.V.: Biocompatibility of biphasic α, β-tricalcium phosphate ceramics in vitro. Bioact. Mater. **5**, 423–427 (2020). https://doi.org/10.1016/j.bioactmat.2020.03.007
20. Cicek, G., Aksoy, E.A., Durucan, C., Hasirci, N.: Alpha-tricalcium phosphate (α-TCP): solid state synthesis from different calcium precursors and the hydraulic reactivity. J. Mater. Sci. Mater. Med. **22**, 809–817 (2011). https://doi.org/10.1007/s10856-011-4283-x
21. Torres, P.M.C., Abrantes, J.C.C., Kaushal, A., Pina, S., Döbelin, N., Bohner, M., Ferreira, J.M.F.: Influence of Mg-doping, calcium pyrophosphate impurities and cooling rate on the allotropic α↔β-tricalcium phosphate phase transformations. J. Eur. Ceram. Soc. **36**, 817–827 (2016). https://doi.org/10.1016/j.jeurceramsoc.2015.09.037
22 Gu, T., Shi, H., Ye, J.: Reinforcement of calcium phosphate cement by incorporating with high-strength β-tricalcium phosphate aggregates. J. Biomed. Mater. Res. - Part B Appl. Biomater. **100 B**, 350–359 (2012). https://doi.org/10.1002/jbm.b.31956
23 Eddy, Tsuchiya, A., Tsuru, K., Ishikawa, K.: Fabrication of self-setting β-TCP granular cement using β-TCP granules and sodium hydrogen sulfate solution. J. Biomater. Appl. **33**, 630–636 (2018). https://doi.org/10.1177/0885328218808015
24. Andrianjatovo, H., Jose, F., Lemaitre, J.: Effect of β-TCP granularity on setting time and strength of calcium phosphate hydraulic cements. J. Mater. Sci. Mater. Med. **7**, 34–39 (1996). https://doi.org/10.1007/BF00121187
25 Torres, P.M.C., Vieira, S.I., Cerqueira, A.R., Pina, S., da Cruz Silva, O.A.B., Abrantes, J.C.C., Ferreira, J.M.F.: Effects of Mn-doping on the structure and biological properties of β-tricalcium phosphate. J. Inorg. Biochem. **136**, 57–66 (2014). https://doi.org/10.1016/j.jinorgbio.2014.03.013
26. Wu, T., Shi, H., Liang, Y., Lu, T., Lin, Z., Ye, J.: Improving osteogenesis of calcium phosphate bone cement by incorporating with manganese doped β-tricalcium phosphate. Mater. Sci. Eng. C. **109**, 110481 (2020). https://doi.org/10.1016/j.msec.2019.110481
27. Rau, J.V., Fadeeva, I.V., Fomin, A.S., Barbaro, K., Galvano, E., Ryzhov, A.P., Murzakhanov, F., Gafurov, M., Orlinskii, S., Antoniac, I., Uskoković, V.: Sic parvis magna: Manganese-substituted tricalcium phosphate and its biophysical properties.

ACS Biomater. Sci. Eng. **5**, 6632–6644 (2019). https://doi.org/10.1021/acsbiomaterials.9b01528

28. Brodziak-Dopierała, B., Kwapuliński, J., Sobczyk, K., Wiechuła, D.: The content of manganese and iron in hip joint tissue. J. Trace Elem. Med. Biol. **27**, 208–212 (2013). https://doi.org/10.1016/j.jtemb.2012.12.005
29. Kamaraj, M., Roopavath, U.K., Giri, P.S., Ponnusamy, N.K., Rath, S.N.: Modulation of 3D printed calcium-deficient apatite constructs with varying Mn concentrations for osteochondral regeneration via endochondral differentiation. ACS Appl. Mater. Interfaces. **14**, 23245–23259 (2022). https://doi.org/10.1021/acsami.2c05110
30. Bae, Y.-J., Kim, M.-H.: Manganese supplementation improves mineral density of the spine and femur and serum osteocalcin in rats. Biol. Trace Elem. Res. **124**, 28–34 (2008). https://doi.org/10.1007/s12011-008-8119-6
31. Strause, L., Saltman, P., Glowacki, J.: The effect of deficiencies of manganese and copper on osteoinduction and on resorption of bone particles in rats. Calcif. Tissue Int. **41**, 145–150 (1987). https://doi.org/10.1007/BF02563794
32. Hreha, J., Wey, A., Cunningham, C., Krell, E.S., Brietbart, E.A., Paglia, D.N., Montemurro, N.J., Nguyen, D.A., Lee, Y.J., Komlos, D., Lim, E., Benevenia, J., O'Connor, J.P., Lin, S.S.: Local manganese chloride treatment accelerates fracture healing in a rat model. J. Orthop. Res. **33**, 122–130 (2015). https://doi.org/10.1002/jor.22733
33. Pabbruwe, M.B., Standard, O.C., Sorrell, C.C., Howlett, C.R.: Bone formation within alumina tubes: Effect of calcium, manganese, and chromium dopants. Biomaterials **25**, 4901–4910 (2004). https://doi.org/10.1016/j.biomaterials.2004.01.005
34. Bracci, B., Torricelli, P., Panzavolta, S., Boanini, E., Giardino, R., Bigi, A.: Effect of Mg2+, Sr2+, and Mn2+ on the chemico-physical and in vitro biological properties of calcium phosphate biomimetic coatings. J. Inorg. Biochem. **103**, 1666–1674 (2009). https://doi.org/10.1016/j.jinorgbio.2009.09.009

35 Barrioni, B.R., Norris, E., Li, S., Naruphontjirakul, P., Jones, J.R., de Pereira, M.M.: Osteogenic potential of sol–gel bioactive glasses containing manganese. J. Mater. Sci. Mater. Med. **30**, 86 (2019). https://doi.org/10.1007/s10856-019-6288-9

36. Wołonciej, M., Milewska, E., Roszkowska-Jakimiec, W.: Trace elements as an activator of antioxidant enzymes. Postepy Hig. Med. Dosw. **70**, 1483–1498 (2016). https://doi.org/10.5604/17322693.1229074
37. Saltman, P.D., Strause, L.G.: The role of trace minerals in osteoporosis. J. Am. Coll. Nutr. **12**, 384–389 (1993). https://doi.org/10.1080/07315724.1993.10718327
38. Zea, C.J., Camci-Unal, G., Pohl, N.L.: Thermodynamics of binding of divalent magnesium and manganese to uridine phosphates: Implications for diabetes-related hypomagnesaemia and carbohydrate biocatalysis. Chem. Cent. J. **2**(15), 1–7 (2008). https://doi.org/10.1186/1752-153X-2-15
39. Li, J., Deng, C., Liang, W., Kang, F., Bai, Y., Ma, B., Wu, C., Dong, S.: Mn-containing bioceramics inhibit osteoclastogenesis and promote osteoporotic bone regeneration via scavenging ROS. Bioact. Mater. **6**, 3839–3850 (2021). https://doi.org/10.1016/j.bioactmat.2021.03.039
40. Röllin, H.B., Nogueira, C.M.C.A.: Manganese: Environmental pollution and health effects, Encycl. Environ. Heal. 617–629 (2011).https://doi.org/10.1016/B978-0-444-52272-6.00540-7
41. Clegg, M.S., Donovan, S.M., Monaco, M.H., Baly, D.L., Ensunsa, J.L., Keen, C.L.: The influence of manganese deficiency on serum IGF-1 and IGF binding proteins in the male rat. Proc. Soc. Exp. Biol. Med. **219**, 41–47 (1998). https://doi.org/10.3181/00379727-219-44314
42. Rondanelli, M., Faliva, M.A., Peroni, G., Infantino, V., Gasparri, C., Iannello, G., Perna, S., Riva, A., Petrangolini, G., Tartara, A.: Essentiality of manganese for bone health: An overview and update. Nat. Prod. Commun. **16**, 1934578X2110166 (2021). https://doi.org/10.1177/1934578X211016649
43. Khatik, R., Wang, Z., Li, F., Zhi, D., Kiran, S., Dwivedi, P., Xu, R.X., Liang, G., Qiu, B., Yang, Q.: "Magnus nano-bullets" as T1/T2 based dual-modal for in vitro and in vivo MRI visualization, Nanomedicine Nanotechnology. Biol. Med. **15**, 264–273 (2019). https://doi.org/10.1016/j.nano.2018.10.005

44 Park, S., Choi, J., Doan, V.H.M., O, S.H.: Biodegradable manganese-doped hydroxyapatite antitumor adjuvant as a promising photo-therapeutic for cancer treatment. Front. Mol. Biosci. **9**, 1085458 (2022). https://doi.org/10.3389/fmolb.2022.1085458

45. Pang, L., Zhao, R., Chen, J., Ding, J., Chen, X., Chai, W., Cui, X., Li, X., Wang, D., Pan, H.: Osteogenic and anti-tumor Cu and Mn-doped borosilicate nanoparticles for syncretic bone repair and chemodynamic therapy in bone tumor treatment. Bioact. Mater. **12**, 1–15 (2022). https://doi.org/10.1016/j.bioactmat.2021.10.030
46. Fu, L.H., Hu, Y.R., Qi, C., He, T., Jiang, S., Jiang, C., He, J., Qu, J., Lin, J., Huang, P.: Biodegradable manganese-doped calcium phosphate nanotheranostics for traceable cascade reaction-enhanced anti-tumor therapy. ACS Nano **13**, 13985–13994 (2019). https://doi.org/10.1021/acsnano.9b05836
47. Rau, J.V., De Bonis, A., Teghil, R., Curcio, M., Fadeeva, I.V., Barbaro, K., Di Menno Di, M., Bucchianico, M., Fosca, Y.Z.: Double substituted with manganese and strontium tricalcium phosphate coatings on zinc-lithium biodegradable alloys for biomedical implant applications. Coatings **13**, 36 (2022). https://doi.org/10.3390/coatings13010036
48. Racette, B.A.: Manganism in the 21st century: The Hanninen lecture. Neurotoxicology **45**, 201–207 (2014). https://doi.org/10.1016/j.neuro.2013.09.007
49. de Moura, T.C., Afadlal, S., Hazell, A.S.: Potential for stem cell treatment in manganism. Neurochem. Int. **112**, 134–145 (2018). https://doi.org/10.1016/j.neuint.2017.10.005
50. O'Neill, R., McCarthy, H.O., Montufar, E.B., Ginebra, M.P., Wilson, D.I., Lennon, A., Dunne, N.: Critical review: Injectability of calcium phosphate pastes and cements. Acta Biomater. **50**, 1–19 (2017). https://doi.org/10.1016/j.actbio.2016.11.019
51. Souza, T.L., Batschauer, A.R., Brito, P.M., Martino-Andrade, A.J., Ortolani-Machado, C.F.: Evaluation of testicular structure in mice after exposure to environmentally relevant doses of manganese during critical windows of development. Ecotoxicol. Environ. Saf. **207**, 111537 (2021). https://doi.org/10.1016/j.ecoenv.2020.111537
52. Rietveld, H.M.: A profile refinement method for nuclear and magnetic structures. J. Appl. Crystallogr. **2**, 65–71 (1969). https://doi.org/10.1107/S0021889869006558
53. Ryu, H.-S., Youn, H.-J., Sun Hong, K., Chang, B.-S., Lee, C.-K., Chung, S.-S.: An improvement in sintering property of β-tricalcium phosphate by addition of calcium pyrophosphate. Biomaterials. **23**, 909–914 (2002). https://doi.org/10.1016/S0142-9612(01)00201-0
54. Turan, Y., Kalkandelen, C., Palaci, Y., Sahin, A., Gokce, H., Gunduz, O., Ben-Nissan, B.: Synthesis and cytotoxicity analysis of porous β-TCP/starch bioceramics. J. Aust. Ceram. Soc. **58**, 487–494 (2022). https://doi.org/10.1007/s41779-022-00702-9
55. Jillavenkatesa, A., Condrate, R.A.: The infrared and raman spectra of β-and α-tricalcium phosphate (Ca $_{3}$ (Po $_{4}$) 2$_{)}$. Spectrosc. Lett. **31**, 1619–1634 (1998). https://doi.org/10.1080/00387019808007439
56. Topsakal, A., Ekren, N., Kilic, O., Oktar, F.N., Mahirogullari, M., Ozkan, O., Sasmazel, H.T., Turk, M., Bogdan, I.M., Stan, G.E., Gunduz, O.: Synthesis and characterization of antibacterial drug loaded β-tricalcium phosphate powders for bone engineering applications. J. Mater. Sci. Mater. Med. **31**, 16 (2020). https://doi.org/10.1007/s10856-019-6356-1
57. Sinusaite, L., Kareiva, A., Zarkov, A.: Thermally induced crystallization and phase evolution of amorphous calcium phosphate

substituted with divalent cations having different sizes. Cryst. Growth Des. **21**, 1242–1248 (2021). https://doi.org/10.1021/acs.cgd.0c01534

58. Szurkowska, K., Szeleszczuk, Ł, Kolmas, J.: Effects of synthesis conditions on the formation of Si-substituted alpha tricalcium phosphates. Int. J. Mol. Sci. **21**, 9164 (2020). https://doi.org/10.3390/ijms21239164
59. Seifert, A., Groll, J., Weichhold, J., Boehm, A.V., Müller, F.A., Gbureck, U.: Phase conversion of ice-templated α-tricalcium phosphate scaffolds into low-temperature calcium phosphates with anisotropic open porosity. Adv. Eng. Mater. **23**, 2001417 (2021). https://doi.org/10.1002/adem.202001417
60. Matsunaga, K., Kubota, T., Toyoura, K., Nakamura, A.: First-principles calculations of divalent substitution of Ca2+ in tricalcium phosphates. Acta Biomater. **23**, 329–337 (2015). https://doi.org/10.1016/j.actbio.2015.05.014
61. Gibson, I.R., Rehman, I., Best, S.M., Bonfield, W.: Characterization of the transformation from calcium-deficient apatite to β-tricalcium phosphate. J. Mater. Sci. Mater. Med. **11**, 533–539 (2000). https://doi.org/10.1023/A:1008961816208
62. Sinusaite, L., Renner, A.M., Schütz, M.B., Antuzevics, A., Rogulis, U., Grigoraviciute-Puroniene, I., Mathur, S., Zarkov, A.: Effect of Mn doping on the low-temperature synthesis of tricalcium phosphate (TCP) polymorphs. J. Eur. Ceram. Soc. **39**, 3257–3263 (2019). https://doi.org/10.1016/j.jeurceramsoc.2019.03.057
63. Renaudin, G., Gomes, S., Nedelec, J.-M.: First-row transition metal doping in calcium phosphate bioceramics: A detailed crystallographic study. Materials (Basel). **10**, 92 (2017). https://doi.org/10.3390/ma10010092
64. Tian, Y., Lu, T., He, F., Xu, Y., Shi, H., Shi, X., Zuo, F., Wu, S., Ye, J.: β-tricalcium phosphate composite ceramics with high compressive strength, enhanced osteogenesis and inhibited osteoclastic activities. Colloids Surf. B Biointerfaces. **167**, 318–327 (2018). https://doi.org/10.1016/j.colsurfb.2018.04.028
65. Lüthen, F., Bulnheim, U., Müller, P.D., Rychly, J., Jesswein, H., Nebe, J.G.B.: Influence of manganese ions on cellular behavior of human osteoblasts in vitro. Biomol. Eng. **24**, 531–536 (2007). https://doi.org/10.1016/j.bioeng.2007.08.003
66. Westhauser, F., Wilkesmann, S., Nawaz, Q., Hohenbild, F., Rehder, F., Saur, M., Fellenberg, J., Moghaddam, A., Ali, M.S., Peukert, W., Boccaccini, A.R.: Effect of manganese, zinc, and copper on the biological and osteogenic properties of mesoporous bioactive glass nanoparticles. J. Biomed. Mater. Res. Part A. **109**, 1457–1467 (2021). https://doi.org/10.1002/jbm.a.37136
67. Miola, M., Brovarone, C.V., Maina, G., Rossi, F., Bergandi, L., Ghigo, D., Saracino, S., Maggiora, M., Canuto, R.A., Muzio, G., Vernè, E.: In vitro study of manganese-doped bioactive glasses for bone regeneration. Mater. Sci. Eng. C. **38**, 107–118 (2014). https://doi.org/10.1016/j.msec.2014.01.045

Authors and Affiliations

Mehmet Can Arpak[1] · Sibel Daglilar[1] · Cevriye Kalkandelen[2,3] · Liliana-Marinela Balescu[4] · Hilal Turkoglu Sasmazel[5] · Iuliana Pasuk[4] · George E. Stan[4] · Kagan Durukan[5] · Oguzhan Gunduz[2,6]

Mehmet Can Arpak
arpakmehmetcan@gmail.com

Sibel Daglilar
dagli@yildiz.edu.tr

Cevriye Kalkandelen
kalkan@iuc.edu.tr

Liliana-Marinela Balescu
liliana.trinca@infim.ro

Hilal Turkoglu Sasmazel
hilal.sasmazel@atilim.edu.tr

Iuliana Pasuk
iuliana.pasuk@infim.ro

George E. Stan
george_stan@infim.ro

Kagan Durukan
kagandurukan@gmail.com

[1] Department of Metallurgical and Materials Engineering, Faculty of Chemical and Metallurgical Engineering, Yildiz Technical University, Istanbul 34220, Turkey

[2] Center for Nanotechnology & Biomaterials Application and Research (NBUAM), Marmara University, 34722 Istanbul, Turkey

[3] Biomedical Devices Technology Department, Vocational School of Technical Sciences, Istanbul University-Cerrahpaşa, 34500 Istanbul, Turkey

[4] National Institute of Materials Physics, 077125 Magurele, Romania

[5] Metallurgical and Materials Engineering Department, Faculty of Engineering, Atilim University, Incek, 06830 Ankara, Turkey

[6] Department of Metallurgical and Materials Engineering, Faculty of Technology, Marmara University, 34722 Istanbul, Turkey